ROYAL SOCIETY
OF CHEMISTRY

PAPER

Check for updates

View Article Online
View Journal | View Issue

Enhancing the thermoelectric performance of donor–acceptor conjugated polymers through dopant miscibility: a comparative study of fluorinated substituents and side-chain lengths†

Jian-Fa Ding,‡[a] Guan-Lin Chen,‡[bcd] Pang-Hsiao Liu,[bcd] Kai-Wei Tseng,[bcd] Wei-Ni Wu,[a] Jhih-Min Lin,[e] Shih-Huang Tung, [ID][b] Leeyih Wang [ID] *[bcd] and Cheng-Liang Liu [ID] *[af]

Conjugated polymers present a compelling option for thermoelectric applications due to their low working temperatures, good compatibility with solution-processing techniques, and high potential for scalability. However, the inherently low electrical conductivities of the pristine conjugated polymers necessitate improvements *via* doping methods. Doping effectively enhances the electrical conductivity by increasing the charge concentration and mobility within the conjugated polymer matrix. Hence, the present study investigates the compatibility between a ferric chloride ($FeCl_3$) dopant and four distinct conjugated polymers and evaluates the effects of the dopant/polymer combination on the thermoelectric properties of the material. First, the influence of backbone engineering is investigated *via* a comparison between 4-(3′,4′-difluoro-3,3″-bis(2-hexyldecyl)-5″-methyl-[2,2′:5′,2″-terthiophen]-5-yl)-7-methylbenzo[c][1,2,5]thiadiazole (**PC16BTF**) and 4-(3,3″-bis(2-hexyldecyl)-5″-methyl-[2,2′:5′,2″-terthiophen]-5-yl)-7-methylbenzo[c][1,2,5]thiadiazole (**PC16BTH**). These polymers differ in that **PC16BTF** incorporates two fluorine-atom substituents on the thiophene ring, while **PC16BTH** contains hydrogen atoms in these positions. Then, the effects of various side-chain lengths are investigated by comparing the abovementioned **PC16BTH** with both 4-(3,3″-bis(2-butyloctyl)-5″-methyl-[2,2′:5′,2″-terthiophen]-5-yl)-7-methylbenzo[c][1,2,5]thiadiazole (**PC12BTH**) and 4-methyl-7-(5″-methyl-3,3″-bis(2-octyldodecyl)-[2,2′:5′,2″-terthiophen]-5-yl)benzo[c][1,2,5]thiadiazole (**PC20BTH**). The $FeCl_3$ dopant was selected for its suitable size and charge transfer capability, which significantly influence the thermoelectric performance of each conjugated polymer. As a result, **PC16BTH** exhibits the highest power factor (PF) of 22.4 $\mu W\ m^{-1}\ K^{-2}$ due to its moderate side-chain length and relatively high doping efficiency. Thus, the present study provides valuable insights into suitable strategies for improving the compatibility between dopants and polymers, thereby offering a promising avenue for further enhancing the thermoelectric performance of doped conjugated polymers.

[a]*Department of Materials Science and Engineering, National Taiwan University, Taipei 10617, Taiwan. E-mail: liucl@ntu.edu.tw*

[b]*Institute of Polymer Science and Engineering, National Taiwan University, Taipei 10617, Taiwan. E-mail: leewang@ntu.edu.tw*

[c]*Center of Atomic Initiative for New Materials, National Taiwan University, Taipei 10617, Taiwan*

[d]*Center for Condensed Matter Sciences, National Taiwan University, Taipei 10617, Taiwan*

[e]*National Synchrotron Radiation Research Center, Hsinchu 30076, Taiwan*

[f]*Advanced Research Center for Green Materials Science and Technology, National Taiwan University, Taipei 10617, Taiwan*

† Electronic supplementary information (ESI) available. See DOI: https://doi.org/10.1039/d4ta00032c

‡ J. F. Ding and G. L. Chen contributed equally to this work.

1 Introduction

The recent escalation in global energy demand has resulted in energy-related concerns for all of humanity. Hence, dependable and sustainable energy sources must be identified in order to address these challenges effectively.[1–3] In this respect, thermoelectricity stands out as a particularly promising energy source, as it enables the conversion of temperature differences into electrical energy without causing additional pollution. With respect to thermoelectric materials, organic/polymeric-based materials have advantages such as remarkably low toxicity and good potential scalability relative to their inorganic counterparts.[2,4–9] Materials for use in thermoelectric devices are commonly evaluated and compared based on the dimensionless figure of merit (*ZT*), which is given by eqn (1):

9806 | *J. Mater. Chem. A*, 2024, **12**, 9806–9816

This journal is © The Royal Society of Chemistry 2024

$$ZT = S^2 \sigma T \kappa^{-1} \quad (1)$$

where S is the Seebeck coefficient, σ is the electrical conductivity, T is the absolute temperature, and κ is the thermal conductivity. However, because organic polymers generally exhibit lower thermal conductivity than inorganic materials, the power factor (PF) is used for a more precise description. This is given by eqn (2):

$$\mathrm{PF} = S^2 \sigma \quad (2)$$

and is expressed in units of $\mu W\ m^{-1}\ K^{-2}$. Thus, the primary challenge in harnessing the full thermoelectric potential of the pristine polymeric material lies in enhancing its inherently low electrical conductivity and, hence, its power factor, which is determined by the charge-carrier mobility and concentration.[10,11] To address this limitation, most studies adopt a strategy of doping the polymers with various additives that enhance the concentration of either the positive or negative charge carriers (referred to as p-type or n-type doping).[12–17] Common p-type dopants include ionic compounds and organic molecules such as ferric chloride ($FeCl_3$) and 2,3,5,6-tetrafluoro-7,7,8,8-tetracyano-quinodimethane (F4TCNQ), while n-type dopants include (4-(1,3-dimethyl-2,3-dihydro-1H-benzoimidazol-2-yl)phenyl)dimethylamine (N-DMBI) The choice of a specific dopant depends on factors such as the energy level and dopant size, as these significantly influence the doping efficiency and charge-carrier concentration.[17] In addition, the doping method is a crucial consideration, and its choice is guided by factors such as the miscibility of the dopant with a given solution and the electrochemical properties of the dopant.

Doped donor–acceptor (D–A) conjugated polymers have attracted substantial attention as a highly promising class of materials for thermoelectric applications.[18–42] The inherent advantages of D–A copolymers lie in their capacity for meticulous property tailoring through the strategic manipulation of molecular structures in both donor and acceptor components. Notably, benzothiadiazole (BT) has emerged as an exemplary acceptor due to its structural rigidity and pronounced electron-withdrawing characteristics.[43,44] Consequently, BT finds widespread use in organic semiconductors, particularly in applications such as organic solar cells and field effect transistors. With the aim of advancing the utility of BT units in thermoelectricity, Liang *et al.* conducted a seminal study exploring various alkyl side-chains of D–A conjugated polymers associated with BT units.[45] The investigation focused on fluorene-containing BT-based conjugated copolymers in which dialkyl side-chains of various lengths were added onto the fluorene-containing units. The results indicated that while the side-chain length had only a limited effect on the Seebeck coefficient, the conjugated polymer with the dodecyl side-chains (designated F12BT) exhibited a notably rougher thin film surface, which significantly impeded the electrical conductivity. By contrast, the shorter side-chain substituent (hexyl; designated F6BT) was found to enhance the thermoelectric performance. As a result, F6BT exhibited a PF of 1.6 $\mu W\ m^{-1}\ K^{-2}$ after doping with $FeCl_3$, which was four times that of the F12BT polymer. More recently, Yoon *et al.* conducted a systematic

investigation into the molecular structure and thermoelectrical properties obtained by introducing various branched alkyl chains to poly(isoindigo-thienothiophene) (PIID-TT) with F4TCNQ as the dopant. The results indicated a trade-off between the side-chain structure and the electrical conductivity in optimizing the thermoelectric performance. Consequently, the maximum power factor of 37.8 $\mu W\ m^{-1}\ K^{-2}$ was achieved by using octyldodecyl side-chains. In addition to side-chain engineering, fluorine substitution has become a prevalent strategy for manipulating the thermoelectric properties of polymeric materials. For example, Wu *et al.* investigated three distinct dopants applied to polymers based on thieno[3,4-*b*]thiophene (TbT) derivatives, both with and without fluorination (PTbTTVT-F and PTbTTVT). The results demonstrated that, regardless of the choice of dopant, the fluorinated polymers exhibited less uniform crystalline orientations and higher Seebeck coefficients after doping. Moreover, the highest PF of 42.8 $\mu W\ m^{-1}\ K^{-2}$ was achieved by the non-fluorinated PTbT after doping which was primarily attributed to an enhanced electrical conductivity. Nevertheless, despite these significant contributions, the combined influence of molecular structure and dopant choice on the thermoelectric performances of closely related materials remains unclear.

Hence, the present study is aimed at addressing this research gap by designing a series of fluorinated and non-fluorinated BT-based D–A conjugated copolymers with various side-chain lengths and examining the respective effects of side-chain length and fluorination on the thermoelectric performance.[46] In addition, the crucial aspect of dopant miscibility is investigated, with the aim of providing a comprehensive understanding of these multifaceted materials for potential applications in sustainable energy generation. The results reveal distinct advantages for each of the synthesized polymers, with the non-fluorinated 12-carbon **PC12BTH** exhibiting the lower activation energy, while the non-fluorinated 20-carbon **PC20BTH** displays exceptional dopant miscibility, and the fluorinated 16-carbon **PC16BTF** exhibits a superior Seebeck coefficient. However, the most favorable overall thermoelectric performance is observed for the non-fluorinated 16-carbon **PC16BTH**, which optimally combines a moderate side-chain length with suitable energy levels. This research establishes an optimized approach to the future design and fabrication of D–A conjugated polymers for use in thermoelectric applications.

2 Results and discussion, experimental

2.1 Synthesis and initial characterization of the various polymers

The synthetic routes of the polymers **PC12BTH**, **PC16BTH**, **PC20BTH**, and **PC16BTF** are outlined in Scheme S1 of the ESI,† where the full synthesis and characterization details are also provided. In brief, 4,7-dibromobenzo[*c*][1,2,5]thiadiazole was subjected to microwave-assisted Stille coupling with three thiophene derivatives with various chain lengths, namely: 4,7-bis(4-(2-

This journal is © The Royal Society of Chemistry 2024

J. Mater. Chem. A, 2024, **12**, 9806–9816 | **9807**

butyloctyl)thiophen-2-yl)benzo[c][1,2,5]thiadiazole, 4,7-bis(4-(2-hexyldecyl)thiophen-2-yl)benzo[c][1,2,5]thiadiazole, and 4,7-bis(4-(2-octyldodecyl)thiophen-2-yl)benzo[c][1,2,5]thiadiazole, with tetrakis(triphenylphosphine)palladium(0) (Pd(PPh$_3$)$_4$) as a catalyst to obtain compounds **1a**, **1b**, and **1c**, respectively. Subsequently, compounds **1a**, **1b**, and **1c** were subjected to bromination with *N*-bromosuccinimide (NBS) at room temperature for 12 h in CHCl$_3$ to yield monomers M1a, M1b, and M1c. The **PC12BTH**, **PC16BTH**, **PC20BTH**, and **PC16BTF** polymers were then synthesized *via* the microwave-assisted Stille coupling copolymerizations of M1a, M1b, and M1c with either 3,4-difluoro-2,5-bis(trimethylstannyl)thiophene (M2) or 2,5-bis(trimethylstannyl)thiophene (M3), with Pd(PPh$_3$)$_4$ as the catalyst. Characterization by gel permeation chromatography (GPC) indicated that the number-average molecular weight (M_n) values of the **PC12BTH**, **PC16BTH**, **PC20BTH**, and **PC16BTF** were found to be 20.6, 26.6, 12.5, and 33.1 kDa, respectively, while the corresponding weight-average molecular weight (M_w) values were 27.2, 37.4, 21.2, and 45.3 kDa. The polydispersity index (PDI) of each polymer was around 1.5, thereby indicating well-controlled polymer synthesis. Moreover, the thermal stability of each polymer is indicated by the thermogravimetric analysis (TGA) results in Fig. S1† Here, the initial decomposition temperatures (T_d or T_{95}) of all four polymers are >400 °C, where T_{95} indicates that only 5% of each polymer has decomposed, and 95% remains. Furthermore, the differential scanning calorimetry (DSC) curves in Fig. S3† clearly demonstrate that fluorination of the polymer structure leads to increases in both the crystallization temperature (T_c) and the melting point (T_m). This, in turn, suggests that fluorination enhances the coplanarity and chain stacking within the polymer.[47,48] Meanwhile, the increase in side-chain length leads to reductions in both T_c and T_m. This is because longer side-chains hinder the development of a finely organized crystalline structure, thus resulting in the formation of disorderly polymer aggregates and the polymer structures are shown in Fig. 1.[49]

2.2 Spectroscopic analyses

The effects of fluorination and side-chain length on the aggregate-state structures of the as-synthesized polymers are revealed by the UV-vis spectra in Fig. S4.† There, the **PC16BTH** and **PC16BTF** polymers exhibit nearly identical absorption patterns, although the main absorption peak exhibits a significant blue shift from 547 nm for **PC16BTH** to 511 nm for **PC16BTF**. This is due to the strong electron-withdrawing nature of the fluorine atom.[50] In these two polymers, the benzothiadiazole segment serves as the
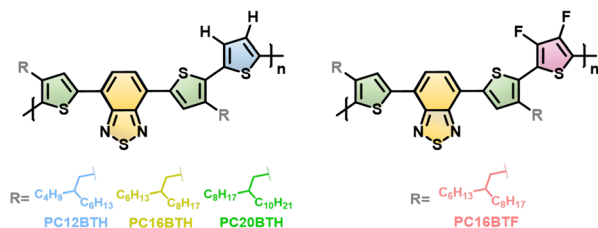
electron acceptor, while the terthiophene segment acts as the electron donor.[51] In the case of **PC16BTF**, however, the electron-withdrawing fluorine atom is situated in the central thiophene ring of the terthiophene donor segment, where it diminishes the electron-donating capacity and, hence, the π-electron delocalization and intramolecular charge transfer ability.[52] Meanwhile, **PC20BTH** exhibits a primary absorption peak at 547 nm (in common with **PC16BTH**), whereas **PC12BTH** exhibits a red shift in the primary peak to 560 nm.[53] This is attributed to reduced steric hindrance of the side-chains, which leads to less torsion in the polymer backbone and, hence, more pronounced interchain interactions.[54,55] For prospective thermoelectric application, deeper insights into the charge transfer processes in the various pristine and doped polymer thin films are provided by the UV-vis-NIR spectra in Fig. 2. Here, each polymer exhibits a primary absorption peak due to intermolecular charge transfer. However, this peak is located at 620, 625, 632, and 630 nm for pristine **PC12BTH** (Fig. 2a), **PC16BTH** (Fig. 2b), **PC20BTH** (Fig. 2c), and **PC16BTF** (Fig. 2d), respectively, due to the effects of fluorination and side-chain length. In addition, the absorption peak of pristine **PC16BTF** exhibits a shoulder at 695 nm (Fig. 2d), which suggests a more pronounced π–π aggregation and, hence, closer arrangement of the polymer chains, due to the fluorination. Furthermore, the optical band gap (E_g^{opt}) of each polymer is derived from the onset absorption wavelength (λ_{onset}) values of the respective thin films, as detailed in the ESI.† The calculation results indicate similar band gap values of 1.59, 1.60, 1.62, and 1.64 eV for pristine **PC12BTH**, **PC16BTH**, **PC20BTH**, and **PC16BTF**, respectively.

Upon doping with FeCl$_3$, the original absorption peak of each polymer exhibits a slight redshift, thereby indicating interactions between the polymers and the dopant. In addition, significant increases in the absorption intensity are observed in the wavelength ranges of 800–1000 nm and 1600–2000 nm, along with an expansion of each absorption range, due to the formation of polaron and bipolaron species, respectively.[56–58] Notably, these polaron and bipolaron signals become more

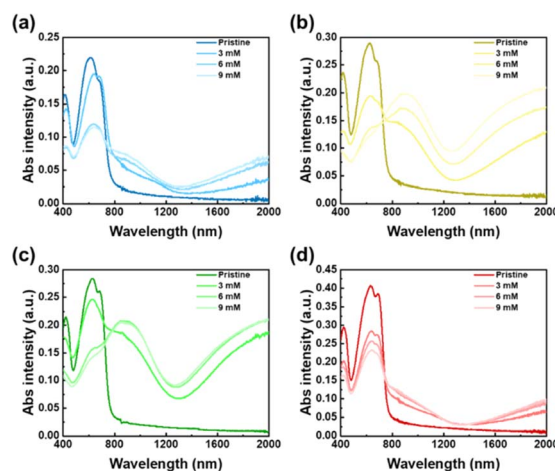Fig. 1 Chemical structure of D−A conjugated polymers used in this study.

Fig. 2 UV-vis-NIR absorption spectra of (a) **PC12BTH**, (b) **PC16BTH**, (c) **PC20BTH**, and (d) **PC16BTF** thin film at the different doping concentrations.
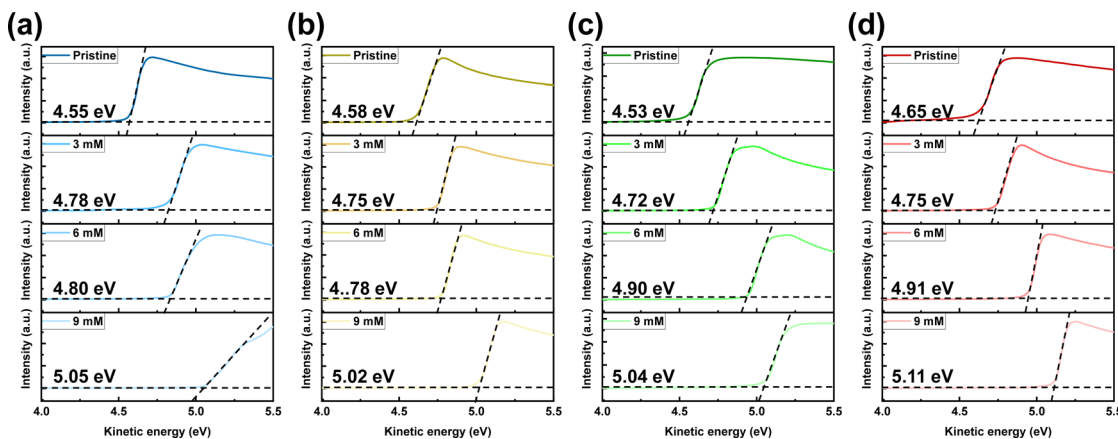
9808 | *J. Mater. Chem. A*, 2024, **12**, 9806–9816

This journal is © The Royal Society of Chemistry 2024

Fig. 3 Low kinetic energy region and the Fermi level of (a) PC12BTH, (b) PC16BTH, (c) PC20BTH, and (d) PC16BTF thin film at the different doping concentrations from UPS.

pronounced as the concentration of dopant is increased. However, **PC16BTH** exhibits more intense polaron and bipolaron peaks than does **PC16BTF**, thereby indicating stronger interactions between the polymer molecules and an enhanced charge transfer ability. Meanwhile, **PC16BTH** and **PC20BTH** exhibit similar spectral characteristics after doping, characterized by a substantial degree of polaron and bipolaron formation, whereas a noticeable reduction in absorption is observed for **PC12BTH**. This can be attributed to the shorter side-chain length of **PC12BTH**, which appears to hinder the compatibility (miscibility) of the dopant and polymer matrix.

Further information on the electronic structures of the as-synthesized conjugated polymers is provided by the ultraviolet photoelectron spectroscopy (UPS) results in Fig. 3. From these results, the Fermi level (E_F) of each polymer can be obtained. The calculated energy levels are presented in Table 1. Thus, the introduction of fluorine is seen to have a noticeable impact on the E_F of pristine **PC16BTF**, giving a significantly lower value of -4.65 eV compared to -4.58 eV for **PC16BTH**. This can be attributed to the strong electron affinity of fluorine, which exerts a significant influence on the overall electronic structure of the conjugated polymer. Meanwhile, the E_F values of the pristine polymers remain relatively stable regardless of the side-chain length. Upon addition of the p-type dopant, however, the E_F values are seen to decrease, as expected. Moreover, the E_F of each doped polymer is seen to decrease as the dopant concentration is increased.[59] This highlights the intricate interplay

between doping concentration and electronic structure, which can have profound implications for the charge-carrier mobility and, hence, the overall performance of the thermoelectric device. The reduction reaction of the dopant and concurrent charge transfer onto the polymer chains are further elucidated by the X-ray photoelectron spectroscopy (XPS) results in Fig. 4. Thus, prior to doping (Fig. 4a), each polymer exhibits a signal at approximately 163 eV from sulfur (S_{2p}, green), along with satellite peaks (yellow and orange) due to residual charge effects.[60] In the case of **PC16BTF**, the S_{2p} peak is observed at a slightly higher energy of 163.4 eV due to the interactions between F and S. However, after p-type doping with a concentration of 6 mM, the S_{2p} peaks of each polymer have shifted towards higher binding energy values because the polymer backbone accepts the positive charge (Fig. 4a). Notably, after doping, the S_{2p} signal of **PC16BTF** shifted 0.2 eV, while that of **PC16BTH** shifted 0.4 eV, thereby indicating that the introduction of fluorine diminishes the influence of the dopant on the polymer. Meanwhile, the Cl XPS results of the doped polymer films (Fig. 4b) indicate peaks in the binding energy range of 196–202 eV, which originate from the $FeCl_3$ dopants.[61–64] When the $FeCl_3$ is dissolved in a solvent, it dissociates into $FeCl_4^-$ and $FeCl_2^+$ ions. When introduced to the polymer, the $FeCl_2^+$ ions are reduced to $FeCl_2$, and Cl^- anions are generated. Due to coulombic interactions, these Cl^- anions coexist with the unreacted $FeCl_4^-$ anions within the polymer chains. Hence, the Cl peak of the doped polymer films can be deconvoluted into

Table 1 Thermal decomposition temperatures (T_d), molecular weight (M_n, M_w), polydispersity index (PDI), onset absorption wavelength (λ_{onset}), and energy level (E_g^{opt}, E_F) of the studied polymers

Polymer	T_d (°C)	M_n (kDa)	M_w (kDa)	PDI	λ_{onset} (nm)	$E_g^{opt a}$ (eV)	E_F (eV)
PC12BTH	445	20.6	27.2	1.32	779	1.59	−4.55
PC16BTH	430	26.6	37.4	1.41	775	1.60	−4.58
PC20BTH	444	12.5	21.2	1.69	765	1.62	−4.53
PC16BTF	401	33.1	45.3	1.36	756	1.64	−4.65

[a] $E_g^{opt} = 1240/\lambda_{onset}$.

This journal is © The Royal Society of Chemistry 2024

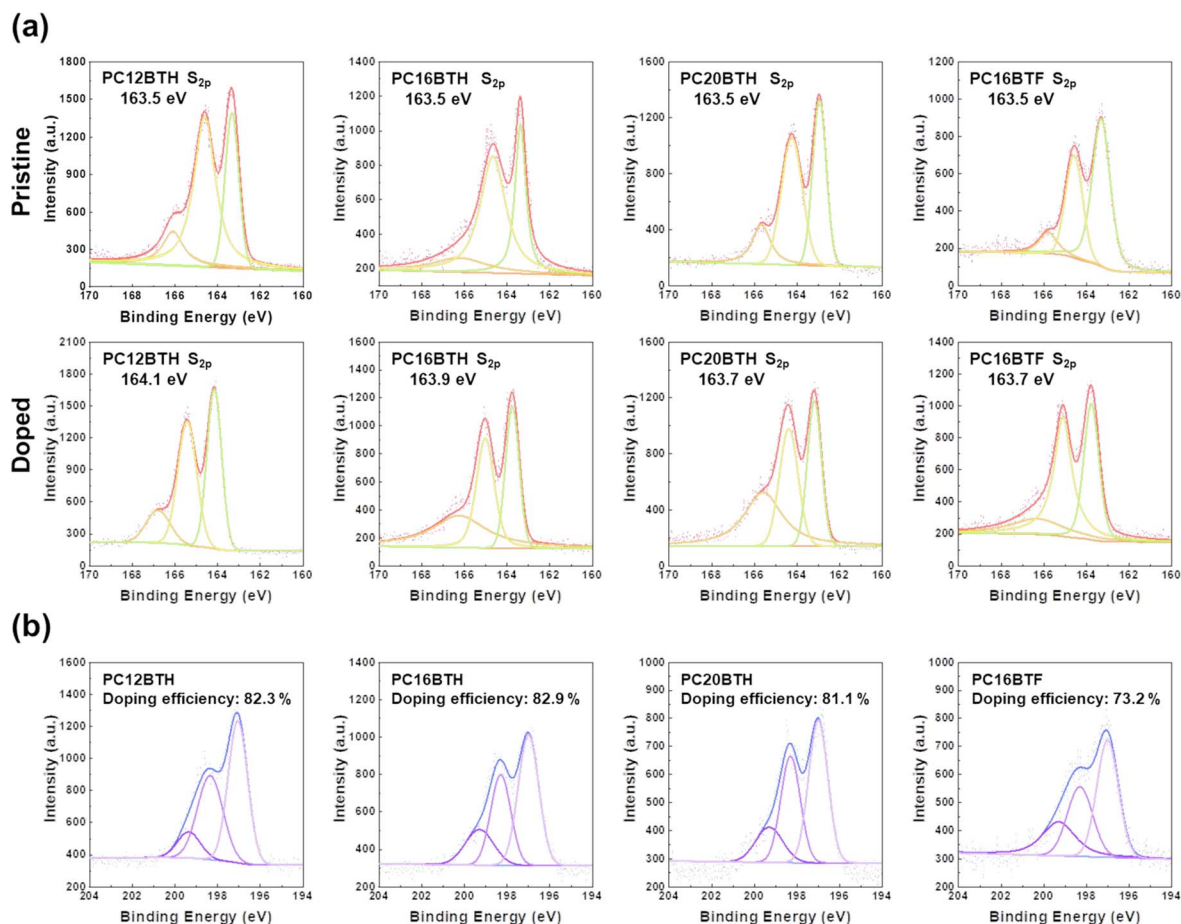J. Mater. Chem. A, 2024, **12**, 9806–9816 | **9809**

Fig. 4 (a) XPS analysis of pristine and 6 mM doped PC16BTF, PC12BTH, PC16BTH, and PC20BTH thin film at the binding energies of the S atoms. (b) XPS analysis of 6 mM doped PC12BTH, PC16BTH, PC20BTH, and PC16BTF thin film at the binding energies of the Cl atoms.

three distinct peaks, including one at 197.0 eV due to the $FeCl_4^-$ and $FeCl_2$ species, along with peaks at 198.3 and 199.3 eV due to the Cl^- and $FeCl_2^+$ ions, respectively. From these results, the doping efficiency (η_d) can be calculated by using eqn (3):[24]

$$\eta_d = \frac{A^-}{A^0 + A^-} \quad (3)$$

where A_0 is the area under the $FeCl_2^+$ peak and A^- is the combined area under the Cl^- and $FeCl_2$ peaks. Thus, as shown in Fig. 4b, the doped PC12BTH, PC16BTH, PC20BTH, and PC16BTF samples have η_d values of 84.3%, 82.9%, 81.1%, and 73.2% respectively. Thus, while there is no significant variation in η_d according to the polymer chain length, PC16BTF exhibits a significantly lower doping efficiency than the other polymers due to the fluorination. This will have important implications for the electrical performance of the fluorinated polymer, as discussed in more detail later. The above results indicate that introducing a dopant into the D–A conjugated polymer leads to a notable change in the chemical states of the elements within the polymer, which can be attributed to the charge transfer processes. This confirms the effectiveness of the doping strategy for modifying the electronic properties of the polymers. Meanwhile, the lower dopant miscibility of the fluorinated polymer

may be explained in terms of hydrophilicity, as demonstrated by comparing the contact angle measurements of the four polymers (Fig. S5†). Thus, PC16BTF exhibits the lowest surface energy (23.4 mN m^{-1}), thereby indicating that the introduction of fluorine increases the hydrophobicity of the polymer. This highlights the importance of considering the chemical structure and hydrophilicity of the dopant when designing materials for thermoelectric applications.

2.3 Morphological and microstructural analyses

The miscibility between the conjugated polymers and $FeCl_3$ dopant is revealed by the atomic force microscopy (AFM) images in Fig. 5. First, we discuss the properties of the four pristine polymers, the pristine PC16BTF surface exhibits distinctive, needle-like self-aggregated structures (Fig. 5d), which result in root-mean-square surface roughness (R_{rms}) of approximately 1.3 nm compared to ~1.2 nm for the three non-fluorinated polymers (Fig. 5a–c). This increase in surface roughness will enable greater contact between the dopant and the PC16BTF matrix, as the valley regions offer ideal sites for dopant deposition, thereby providing a substantial surface area for the dopant molecules. In the comparison of different side chain lengths, the only discernible effect of increasing side-chain length is a slight
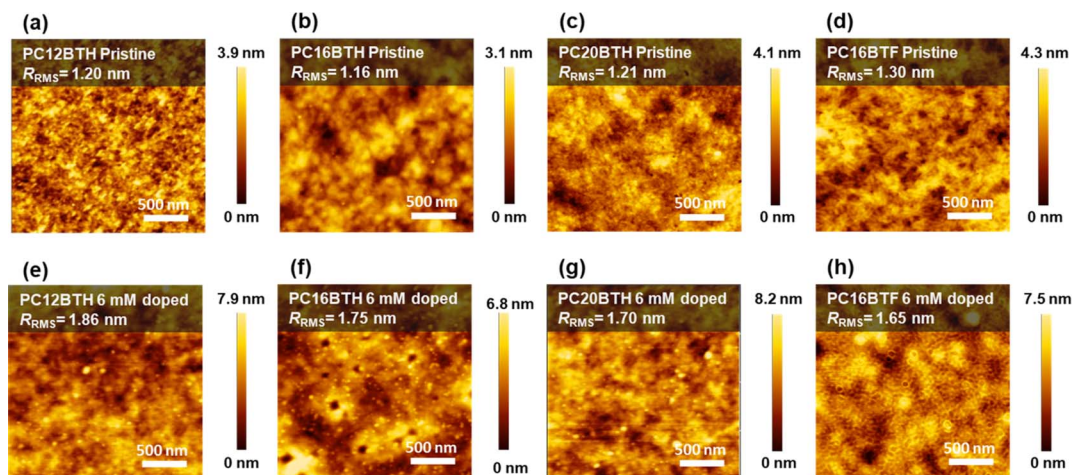
9810 | J. Mater. Chem. A, 2024, 12, 9806–9816

This journal is © The Royal Society of Chemistry 2024

Fig. 5 AFM height images and the root-mean-square surface roughness (R_{rms}) of (a–d) pristine and (e–h) after 6 mM FeCl$_3$ doped polymer.

increase in surface roughness. This can be attributed to the molecular packing within the pristine polymer, and will be discussed later. Moving on to the discussion of doped polymers, after doping, there are white dots on the surfaces of all polymers. As the doping concentration increases, more white dots are formed. Therefore, we speculate that these white dots are caused by the precipitation of the dopant.[65] These precipitates may also act as potential obstacles during charge transport, thereby contributing to a reduction in conductivity.[66] For the cases of all four polymers, the surface roughness increases after doping due to the precipitation. For example, this results in an increase in the R_{rms} from 1.2 for pristine to 1.76 nm after 6 mM doped in the **PC12BTH** thin film. Furthermore, in the discussion of roughness, under the same doping concentration for non-fluorinated polymers, more precipitation indicates poorer miscibility between the dopant and the polymer, leading to increase of roughness. From here, the better miscibility of **PC20BTH** is proved, under 6 mM doping concentration, **PC20BTH** has lower roughness than the other two non-fluorinated polymers. However, **PC16BTF** demonstrates the lowest roughness, this is caused by the needle-like surface mentioned before. The dopant precipitation locates at the valley region, leading to less increase in the roughness.

Meanwhile, the vertical distribution of the FeCl$_3$ dopant within the polymer thin film is revealed by the XPS depth analysis in Fig. 6. Here, the doped **PC12BTH** and BC16BTH (Fig. 6a and b) exhibit significant dopant concentrations near their surfaces, while the Cl signals gradually decrease with increasing film depth. By contrast, the doped **PC20BTH** exhibits a distinctly uniform distribution of dopant throughout its depth. This can be attributed to the longer side-chains within this polymer structure, which increase the intermolecular distance and facilitate the diffusion of dopant molecules through the film.[9,50] Meanwhile, the doped **PC16BTF** also exhibits a uniform distribution of dopant throughout the film, despite the shorter side-chains compared to **PC20BTH**, due to the specific morphology provided by fluorination.[9] In agreement with the above AFM results, these XPS results demonstrate the considerable role of polymer morphology and microstructure in controlling the dopant distribution.

The microstructures of the as-synthesized polymers are further revealed by the grazing-incidence wide-angle X-ray scattering (GIWAXS) results for the pristine and 6 mM FeCl$_3$ doped polymers in Fig. 7, and schematic diagrams of the interpreted structures are presented in Fig. 8. Thus, the pristine **PC12BTH** exhibits primarily edge-on stacking (Fig. 7a), whereas **PC16BTH** (Fig. 7b) and **PC20BTH** (Fig. 7c) exhibit a combination of edge-on and face-on stacking. This is because the longer side-chains are more likely to lie on the substrate, thereby generating the face-on arrangement. However, **PC16BTF** is predominately oriented in a face-on manner, as shown in Fig. 7d, thereby demonstrating that the molecular stacking is significantly influenced by the presence of fluorine atoms on the polymer backbone. Based on the above GIWAXS analysis, the lattice spacing (d-spacing), peak full width at half maximum (FWHM), and coherent length (L_c) values of the pristine and doped polymers are listed in Table 2. Thus, the increase in side-chain length leads to lamellar spacings of 21.0, 21.6, and 22.2 Å for the pristine **PC12BTH**, **PC16BTH**, and **PC20BTH**, respectively. Along with the abovementioned variation
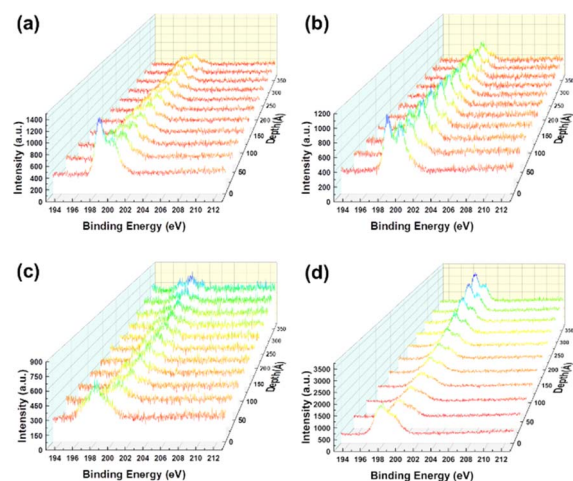

Fig. 6 XPS depth spectra at the binding energies of the Cl atoms after 6 mM FeCl$_3$ doped for (a) **PC12BTH**, (b) **PC16BTH**, (c) **PC20BTH**, and (d) **PC16BTF** film.
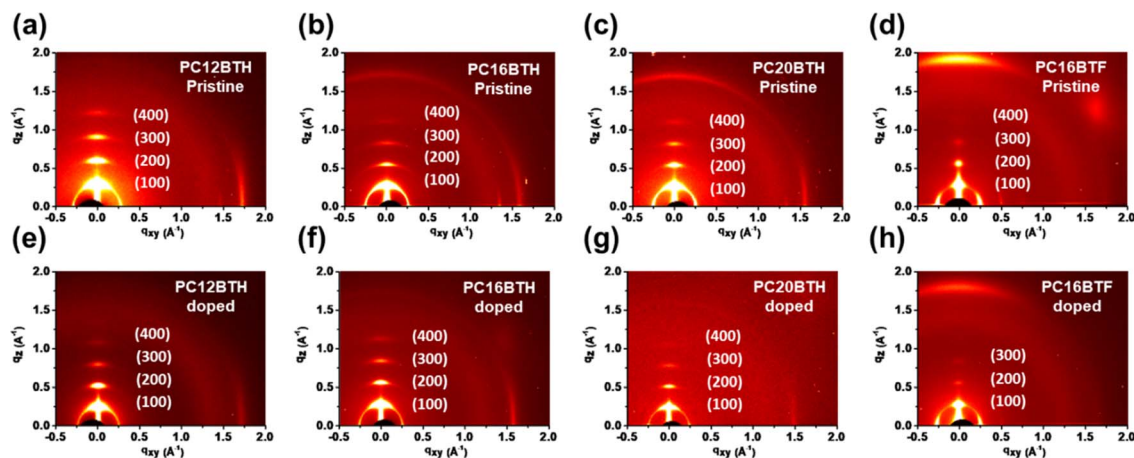
This journal is © The Royal Society of Chemistry 2024

J. Mater. Chem. A, 2024, **12**, 9806–9816 | **9811**

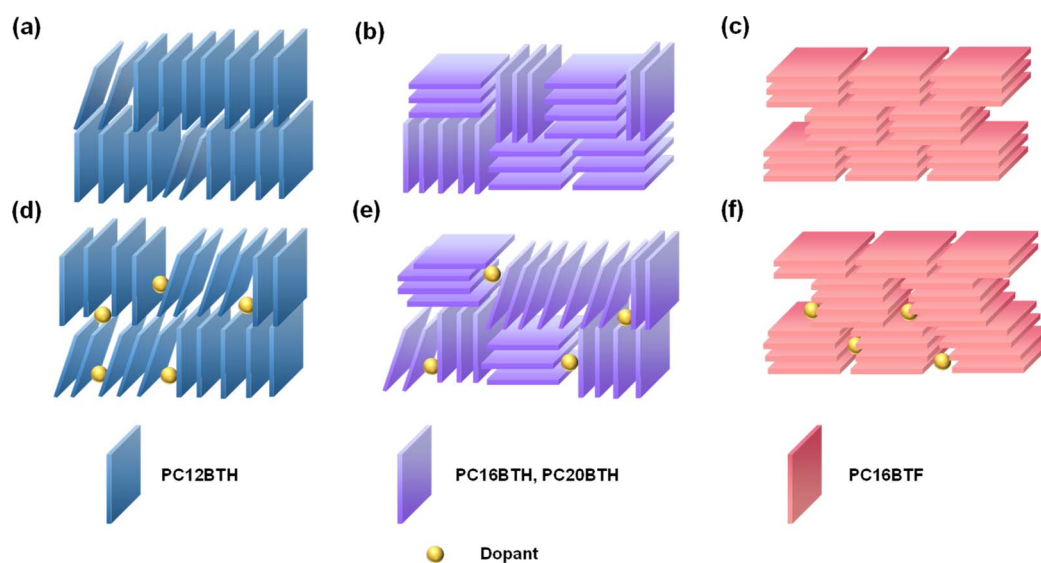Fig. 7   2D-GIWAXS patterns of polymer films: (a–d) pristine and (e–h) after 6 mM FeCl₃ doped polymers.

Fig. 8   Illustration of the orientation of (a) pristine **PC12BTH**, (b) pristine **PC16BTH** and **PC20BTH**, (c) pristine **PC12BTH**, (d) doped **PC12BTH**, (e) doped **PC16BTH** and **PC20BTH**, (f) doped **PC16BTF**.

in molecular stacking, this variation in spacing highlights the importance of side-chain length in modulating the structure of the polymer thin film. This, in turn, will affect the charge transport ability and performance of the corresponding thermoelectric device. Furthermore, the inclusion of fluorine atoms on the polymer backbone leads to a significant decrease in the lamellar and π–π spacings, from 21.6 Å and 3.47 Å, respectively, for the pristine **PC16BTH** to 20.4 Å and 3.41 Å, respectively, for **PC16BTF**.[67] This can be attributed to the robust coulombic forces of the fluorine atoms and has the potential to improve charge-carrier transport.

After doping, the molecular packing configurations of the conjugated polymer films are shown schematically in Fig. 8a. Here, **PC12BTH** (Fig. 7e) retains its edge-on configuration, and **PC16BTF** (Fig. 7h) retains its face-on configuration. However, the combination of edge-on and face-on stacking in the pristine **PC16BTH** and **PC20BTH** becomes predominantly edge-on after

doping (Fig. 7f and g, respectively). Furthermore, after doping, the molecular spacings all increase due to the intercalation of the dopants. Thus, the lamellar spacing of **PC16BTH** increases from 21.6 Å before doping to 22.5 Å afterward, while the π–π spacing increases from 3.47 to 3.53 Å (Table 2). Notably, the difference between the lamellar spacing of **PC16BTF** before and after doping is only ~0.8 Å compared to differences of ~1.1 Å for the other three polymers. This suggests that the molecular stacking of the **PC16BTF** is less distorted than that of the non-fluorinated polymers due to the stronger molecular interactions in **PC16BTF**. Meanwhile, the coherent lengths of the pristine **PC12BTH**, **PC16BTH**, **PC20BTH**, and **PC16BTF** films are 307.7 Å, 380.1 Å, 294.5 Å, and 210.4 Å, respectively (Table 2). These lengths are related to the crystallite size of each polymer; hence, the results indicate that the fluorinated polymer (**PC16BTF**) has the smallest crystallites among the four polymers.

9812 | *J. Mater. Chem. A*, 2024, **12**, 9806–9816

This journal is © The Royal Society of Chemistry 2024

Table 2 Crystallographic parameters of pristine and doped polymers

Polymers		π–π (010) spacing (Å)	Lamellar (100) spacing (Å)	FWHM (100) (Å^{-1})	L_c (100) (Å)
PC12BTH	Pristine	3.46	21.0	0.030	307.7
	Doped	3.51	22.4	0.032	275.8
PC16BTH	Pristine	3.47	21.6	0.028	380.1
	Doped	3.53	22.5	0.033	269.0
PC20BTH	Pristine	3.56	22.2	0.031	294.5
	Doped	3.69	23.3	0.037	195.1
PC16BTF	Pristine	3.41	20.4	0.038	210.4
	Doped	3.46	21.2	0.039	191.9

2.4 Charge transport properties

The charge transport properties of the as-synthesized polymers after doping with 6 mM FeCl$_3$ are revealed by the Hall effect measurements in Table S1.† Thus, the doped **PC16BTF** exhibits a notably elevated charge-carrier mobility of 4.75×10^{-2} cm^2 V^{-1} s^{-1} due to the stronger molecular interactions and shorter molecular distances observed in the above mentioned GIWAXS results. Moreover, the effect of side-chain length on the charge-carrier mobility is clearly evident, with **PC12BTH**, **PC16BTH**, and **PC20BTH** exhibiting mobilities of 3.71×10^{-2}, 3.56×10^{-2}, and 3.04×10^{-2} cm^2 V^{-1} s^{-1}, respectively. This can be correlated with the side-chain orientations obtained from the GIWAXS analysis, with a more uniform orientation leading to decreased charge-carrier scattering and increased mobility. However, in the absence of a conjugated component, longer side-chains tend to impede the charge-carrier transport and provide spaces for dopant interception, thus leading to increased charge-carrier concentrations compared to the shorter side-chains.[54] Furthermore, moving on to the discussion of carrier concentration, the polymer **PC20BTH**, distinguished by longer side chains, provides more space for dopant molecules to reside between polymer chains. This expanded spatial accommodation enhances the potential for charge transfer, leading to higher carrier concentrations under 6 mM doping concentration compared to others. Additionally, when comparing polymers with similar side chain lengths, it becomes apparent that **PC16BTF** demonstrates a lower carrier concentration. This difference is attributed to the markedly lower doping efficiency of **PC16BTF** compared to **PC16BTH**. Consequently, the optimal side-chain length for electrical conductivity must be identified. With this in mind, further insights into the semiconductor properties of the various doped polymers can be gained by calculating the activation energy (E_a) of each polymer.[62] This can be obtained by measuring the electrical conductivity (σ) at various temperatures, and plugging the results into eqn (4):

$$\sigma = \sigma_{max} \exp\left(\frac{-E_a}{k_B T}\right) \qquad (4)$$

where σ_{max} is the maximum conductivity at 323 K, k_B is Boltzmann's constant, and T is the absolute temperature. The fitting results in Fig. S8† indicate E_a values of 87, 91, 101, and 121 meV for **PC12BTH**, **PC16BTH**, **PC20BTH**, and **PC16BTF**, respectively.

The higher activation energy of **PC16BTF** is attributed to the electron-withdrawing ability from the fluorine on the thiophene, which impedes electron delocalization. Meanwhile, among the three non-fluorinated 6 mM doped polymers, **PC12BTH** exhibits the lowest activation energy which matches the mobility result in the Hall effect measurement. Notably, the consistent trends in the Hall effect and electrical conductivity measurements highlight the intricate relationship between charge-carrier mobility and concentration.

2.5 Thermoelectric properties

The thermoelectric characteristics of the various polymers are revealed by their Seebeck coefficients, electrical conductivities, and PF values in Fig. 9. Here, the lower doping efficiency and charge-carrier concentration of **PC16BTF** cause its electrical conductivity to remain lower than that of the other three doped polymers at all doping concentrations (Fig. 9d), despite the higher charge-carrier mobility provided by its reduced lamellar spacing. For instance, the 6 mM FeCl$_3$ doped **PC16BTF** exhibits a conductivity of only 72.1 S cm^{-1} compared to 118.7 S cm^{-1} for the non-fluorinated polymer with the same chain length (**PC16BTH**) at the same doping concentration. Meanwhile, the effect of side-chain length is demonstrated by electrical conductivity values of 76.3, 118.7, and 98.4 S cm^{-1} for the 6 mM FeCl$_3$ doped **PC12BTH**, **PC16BTH**, and **PC20BTH**, respectively. Furthermore, at reasonably low concentrations, the electrical conductivity of each polymer is seen to increase with the increase in doping concentration. However, once the doping concentration exceeds 7.5 mM, the charge-carrier concentration becomes saturated, and no further change in electrical conductivity is observed when the doping concentration is further increased. Given that the electrical conductivity is directly proportional to the charge-carrier mobility and concentration, these results, combined with the Hall effect measurements, confirm that the optimal side-chain length for the D–A conjugated polymer is achieved with **PC16BTH**. The results in Fig. 9 also illustrate the fundamental trade-off relationship between the Seebeck coefficient and the electrical conductivity. The Seebeck coefficient is intrinsically linked to the charge-carrier concentration, as described in eqn (5):

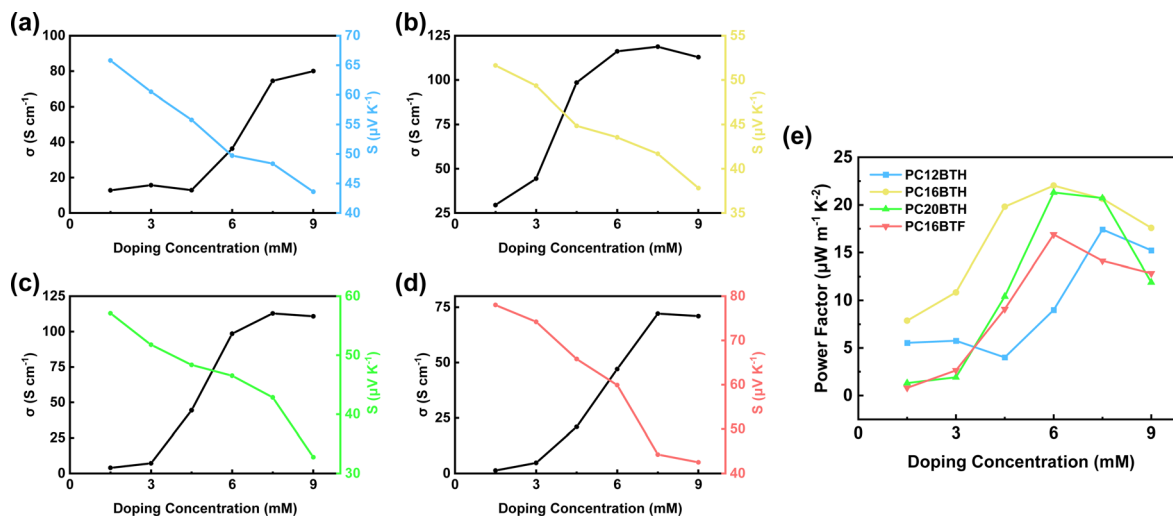$$S = \frac{8\pi^2 k_B^2 T}{3eh^2} m \left(\frac{\pi}{3n}\right)^{\frac{2}{3}} \qquad (5)$$

This journal is © The Royal Society of Chemistry 2024

J. Mater. Chem. A, 2024, **12**, 9806–9816 | **9813**

Fig. 9 Line chart of electrical conductivity (σ) and Seebeck coefficient (S) of doped (a) **PC12BTH**, (b) **PC16BTH**, (c) **PC20BTH**, (d) **PC16BTF** film at varying doping concentrations. (e) Comparison of the power factor of four doped polymer films at varying doping concentrations.

where k_B is Boltzmann's constant, T is the absolute temperature, e is the electron charge, m is the mass of electrons, and n is the charge-carrier concentration.[4,58] Hence, the trade-off between the Seebeck coefficient and electrical conductivity arises from the reciprocal relationship between the Seebeck coefficient and the charge-carrier concentration.[9,68] The results in Fig. 7d indicate that the 6 mM FeCl$_3$ doped **PC16BTF** has the highest Seebeck coefficient of 59.9 μV K^{-1} compared to 45–50 μV K^{-1} for the other polymers at the same doping concentration. This is attributed to the lower charge-carrier concentration in **PC16BTF**, as evidenced by the Hall effect measurements.

As noted in the Introduction, materials for use in thermoelectric devices are commonly evaluated and compared on the basis of the dimensionless figure of merit (ZT), which is given as eqn (1). This equation can be rearranged to indicate an inverse relationship between the Seebeck coefficient and the thermal conductivity.[9] From a structural point of view, thermal conduction can occur *via* two primary pathways, namely: electron transport and lattice vibration.[4,17] In thin film materials, lattice vibrations, commonly referred to as phonons, typically serve as the primary pathway for heat conduction. In this respect, increased microstructural order is often associated with enhanced phonon transport efficiency. Consequently, a well-established crystallinity is frequently correlated with superior thermal conductivity and, hence, a decreased Seebeck coefficient. The results in Fig. 9a–c indicate that the Seebeck coefficients of the 6 mM FeCl$_3$ doped **PC12BTH**, **PC16BTH**, and **PC20BTH** films are 49.7, 43.5, and 46.5 μV K^{-1}, respectively, thereby demonstrating that the side-chain length has minimal impact on the Seebeck coefficient. However, the Seebeck coefficient clearly decreases with the increase in doping concentration due to the reciprocal relationship between charge-carrier concentration and the Seebeck coefficient.

Taken together, the results of this study demonstrate that **PC16BTH** exhibits the most favorable thermoelectric performance, with a higher doping efficiency and charge-carrier

concentration than the equivalent fluorinated polymer (**PC16BTF**). Thus, the superior Seebeck coefficient of **PC16BTF** is not sufficient to compensate for its lower electrical conductivity. Moreover, the optimal side-chain length of **PC16BTH** leads to better charge-carrier mobility and charge-carrier concentrations relative to those of **PC12BTH** and **PC20BTH**. Upon doping with 6 mM FeCl$_3$, the electrical conductivity and Seebeck coefficient of **PC16BTH** are 118.7 S cm^{-1} and 43.5 μV K^{-1}, respectively, yielding the highest power factor of 22.4 μW m^{-1} K^{-2} due to the moderate side-chain length and sufficiently high doping efficiency. These results highlight the intricate interplay between the molecular structure, thin film morphology, and choice of dopant in the pursuit of optimized polymer-based thermoelectric materials.

3 Conclusions

The present study highlighted the influence of side-chain length and polymer-backbone fluorination on the film morphology, dopant miscibility, charge transfer dynamics, and charge-carrier mobility in materials for use in thermoelectric devices. For example, valuable insights into the charge transfer processes after doping with FeCl$_3$, were provided by ultraviolet-visible-near infrared (UV-vis-NIR) spectrometry. These results demonstrated that fluorine substitution leads to decreased absorption, while the side-chain length influences the formation of polarons and bipolarons. In addition, an ultraviolet photoelectron spectroscopy (UPS) analysis indicated that the strong affinity of the substituted fluorine atoms tended to lower the energy of the Fermi level (E_F). Meanwhile, an X-ray photoelectron spectroscopy (XPS) analysis highlighted the different chemical states of the various polymers, which were manifested as shifts in the binding energy and variations in the doping efficiency. Furthermore, the morphologies and microstructures of the various polymers were examined by atomic force microscopy (AFM) and grazing-incidence wide-angle X-ray

9814 | *J. Mater. Chem. A*, 2024, **12**, 9806–9816

This journal is © The Royal Society of Chemistry 2024

scattering (GIWAXS). The results indicated that the presence of fluorine in the polymer backbone contributes to surface aggregation, while the side-chain length affects the dopant–polymer miscibility. In addition, the GIWAXS analysis revealed variations in the molecular packing distances and orientations, thereby offering valuable insights into the charge transport mechanisms. Notably, the GIWAXS results were consistent with the Hall effect measurements and ultimately revealed that the fluorinated polymer with a chain length of 16 carbon atoms (designated **PC16BTF**) exhibits outstanding mobility compared to its non-fluorinated counterpart (*i.e.*, **PC16BTH**). Nevertheless, the non-fluorinated **PC16BTH** exhibited the best thermoelectric performance, with a superior power factor of 22.4 $\mu W\ m^{-1}\ K^{-2}$, due to the trade-off relationship between the Seebeck coefficient and electrical conductivity. This demonstrates the pivotal role of chemical composition and microstructural considerations in the development of doped polymer thermoelectric materials. In brief, the comprehensive study presented herein provides a valuable guideline for the design and synthesis of doped conjugated polymers for use in thermoelectric applications, with a particular emphasis on enhancing the thermoelectric properties *via* judicious chemical substitution and side-chain engineering.

Author contributions

J. F. Ding and G. L. Chen executed the experiment and wrote the manuscript. P. H. Liu and K. W. Tseng measured the spectroscopic properties. J. M. Lin and S. H. Tung gave assistance on GIWAXS data analysis, L. Wang and C. L. Liu revised the manuscript.

Conflicts of interest

There are no conflicts to declare.

Acknowledgements

Notes and references

1 M. Goel and M. Thelakkat, *Macromolecules*, 2020, **53**, 3632–3642.
2 M. Massetti, F. Jiao, A. J. Ferguson, D. Zhao, K. Wijeratne, A. Wurger, J. L. Blackburn, X. Crispin and S. Fabiano, *Chem. Rev.*, 2021, **121**, 12465–12547.
3 L. Deng and G. Chen, *Nano Energy*, 2021, **80**, 105448.
4 W. Zhao, J. Ding, Y. Zou, C. A. Di and D. Zhu, *Chem. Soc. Rev.*, 2020, **49**, 7210–7228.
5 F. Zhang and C.-a. Di, *Chem. Mater.*, 2020, **32**, 2688–2702.
6 S. Xu, X.-L. Shi, M. Dargusch, C. Di, J. Zou and Z.-G. Chen, *Prog. Mater. Sci.*, 2021, **121**, 100840.
7 J. Wang, L. Liu, F. Wu, Z. Liu, Z. Fan, L. Chen and Y. Chen, *ChemSusChem*, 2022, **15**, e202102420.
8 Y. Zhang, W. Wang, F. Zhang, K. Dai, C. Li, Y. Fan, G. Chen and Q. Zheng, *Small*, 2022, **18**, 2104922.
9 S. Wang, G. Zuo, J. Kim and H. Sirringhaus, *Prog. Polym. Sci.*, 2022, **129**, 101548.
10 H. Chai, Z. Xu, H. Li, F. Zhong, S. Bai and L. Chen, *ACS Appl. Electron. Mater.*, 2022, **4**, 4947–4954.
11 J. Li, A. B. Huckleby and M. Zhang, *J. Mater.*, 2022, **8**, 204–220.
12 A. Tripathi, Y. Lee, S. Lee and H. Y. Woo, *J. Mater. Chem. C*, 2022, **10**, 6114–6140.
13 T. L. D. Tam and J. Xu, *J. Mater. Chem. A*, 2021, **9**, 5149–5163.
14 Y. Lu, J. Y. Wang and J. Pei, *Acc. Chem. Res.*, 2021, **54**, 2871–2883.
15 J. Liang, S. Yin and C. Wan, *Annu. Rev. Mater. Res.*, 2020, **50**, 319–344.
16 J. T. Li and T. Lei, *Chem.–Asian J.*, 2021, **16**, 1508–1518.
17 J. Tang, Y.-H. Pai and Z. Liang, *ACS Energy Lett.*, 2022, **7**, 4299–4324.
18 H. J. Cheon, T. S. Lee, J. E. Lee, S. B. Kim, E. H. Suh, S.-K. Kwon, Y. J. Jeong, J. Jang and Y.-H. Kim, *Chem. Mater.*, 2023, **35**, 1796–1805.
19 B. Li, X. Li, F. Yang, Y. Chen, X. Mao, S. Wan, H. Xin, S. Yan, M. Wang, C. Gao and L. Wang, *ACS Appl. Energy Mater.*, 2021, **4**, 4662–4671.
20 F. Zhong, X. Yin, J. Wu, C. Gao, C. Zhong and L. Wang, *J. Mater. Chem. A*, 2022, **10**, 18030–18037.
21 Q. He, T. L. D. Tam, X. Q. Koh, N. N. Tham, H. Meng, W. Huang and J. Xu, *J. Mater. Chem. C*, 2023, **11**, 204–210.
22 W.-N. Wu, K.-i. Sato, J.-H. Fu, Y.-T. Chan, J.-M. Lin, S.-H. Tung, T. Higashihara and C.-L. Liu, *J. Mater. Chem. A*, 2023, **11**, 17091–17100.
23 A. Tripathi, Y. Lee, C. Jung, S. Kim, S. Lee, W. Choi, C. Park, Y. W. Kwon, H. Lee and H. Y. Woo, *J. Mater. Chem. C*, 2023, **11**, 5646–5656.
24 C.-H. Tsai, Y.-C. Lin, W.-N. Wu, S.-H. Tung, W.-C. Chen and C.-L. Liu, *J. Mater. Chem. C*, 2023, **11**, 6874–6883.
25 S. Deng, C. Dong, J. Liu, B. Meng, J. Hu, Y. Min, H. Tian, J. Liu and L. Wang, *Angew. Chem., Int. Ed.*, 2023, **62**, e202216049.
26 K. Feng, J. Wang, S. Y. Jeong, W. Yang, J. Li, H. Y. Woo and X. Guo, *Adv. Sci.*, 2023, **10**, e2302629.

This journal is © The Royal Society of Chemistry 2024

J. Mater. Chem. A, 2024, **12**, 9806–9816 | **9815**

27 S. A. Gregory, A. Atassi, J. F. Ponder Jr, G. Freychet, G. M. Su, J. R. Reynolds, M. D. Losego and S. K. Yee, *J. Phys. Chem. C*, 2023, **127**, 12206–12217.

28 J. Han, Y. Song, N. Chen, A. Chiu, P. M. McGuiggan, N. Adams, S. M. Thon, J. D. Tovar and H. E. Katz, *ACS Mater. Lett.*, 2022, **4**, 1139–1145.

29 Q. He, T. L. D. Tam, T. Lin, S. W. Chien, M. Lin, H. Meng, W. Huang and J. Xu, *ACS Macro Lett.*, 2022, **11**, 1136–1141.

30 J. Li, K. Yang, D. Wang, B. Liu, Y. Wang, S. Y. Jeong, Z. Chen, H. Y. Woo and X. Guo, *Macromolecules*, 2023, **56**, 2339–2347.

31 J. Liu, Y. Shi, J. Dong, M. I. Nugraha, X. Qiu, M. Su, R. C. Chiechi, D. Baran, G. Portale, X. Guo and L. J. A. Koster, *ACS Energy Lett.*, 2019, **4**, 1556–1564.

32 T. L. Dexter Tam, A. Moudgil, W. J. Teh, Z. M. Wong, A. D. Handoko, S. W. Chien, S. W. Yang, B. S. Yeo, W. L. Leong and J. Xu, *J. Phys. Chem. B*, 2022, **126**, 2073–2085.

33 S. Riera-Galindo, A. O. Biroli, A. Forni, Y. Puttisong, F. Tessore, M. Pizzotti, E. Pavlopoulou, E. Solano, S. Wang, G. Wang, T. P. Ruoko, W. M. Chen, M. Kemerink, M. Berggren, G. di Carlo and S. Fabiano, *ACS Appl. Mater. Interfaces*, 2019, **11**, 37981–37990.

34 Y. Song, X. Dai, Y. Zou, C. Li, C. A. Di, D. Zhang and D. Zhu, *Small*, 2023, **19**, e2300231.

35 Y. Song, J. Ding, X. Dai, C. Li, C.-a. Di and D. Zhang, *ACS Mater. Lett.*, 2022, **4**, 521–527.

36 T. L. D. Tam, C. K. Ng, S. L. Lim, E. Yildirim, J. Ko, W. L. Leong, S.-W. Yang and J. Xu, *Chem. Mater.*, 2019, **31**, 8543–8550.

37 X. Yan, M. Xiong, J. T. Li, S. Zhang, Z. Ahmad, Y. Lu, Z. Y. Wang, Z. F. Yao, J. Y. Wang, X. Gu and T. Lei, *J. Am. Chem. Soc.*, 2019, **141**, 20215–20221.

38 A. Hochgesang, A. Erhardt, J. Mohanraj, M. Kuhn, E. M. Herzig, S. Olthof and M. Thelakkat, *Adv. Funct. Mater.*, 2023, **33**, 2300614.

39 J. Min, D. Kim, S. G. Han, C. Park, H. Lim, W. Sung and K. Cho, *Adv. Electron. Mater.*, 2022, **8**, 2101142.

40 A. Tripathi, B. E. Seo, M. J. Kim, Y. Lee, S. Lee, S. E. Yoon, U. J. Kim, Y. W. Kwon, H. Seo, K. Kwak, J. H. Kim and H. Y. Woo, *Adv. Electron. Mater.*, 2022, **8**, 2200456.

41 J. Tang, J. Ji, R. Chen, Y. Yan, Y. Zhao and Z. Liang, *Adv. Sci.*, 2022, **9**, e2103646.

42 H. Li, J. Song, J. Xiao, L. Wu, H. E. Katz and L. Chen, *Adv. Funct. Mater.*, 2020, **30**, 2004378.

43 S. Fratini, M. Nikolka, A. Salleo, G. Schweicher and H. Sirringhaus, *Nat. Mater.*, 2020, **19**, 491–502.

44 S. Ming, S. Zhen, K. Lin, L. Zhao, J. Xu, B. Lu, L. Wang, J. Xiong and Z. Zhu, *J. Electron. Mater.*, 2014, **44**, 1606–1613.

45 A. Liang, X. Zhou, W. Zhou, T. Wan, L. Wang, C. Pan and L. Wang, *Macromol. Rapid Commun.*, 2017, **38**, 1600817.

46 V. Vijayakumar, E. Zaborova, L. Biniek, H. Zeng, L. Herrmann, A. Carvalho, O. Boyron, N. Leclerc and M. Brinkmann, *ACS Appl. Mater. Interfaces*, 2019, **11**, 4942–4953.

47 F. Wang, Y. Dai, W. Wang, H. Lu, L. Qiu, Y. Ding and G. Zhang, *Chem. Mater.*, 2018, **30**, 5451–5459.

48 J. Oh, K. Kranthiraja, C. Lee, K. Gunasekar, S. Kim, B. Ma, B. J. Kim and S.-H. Jin, *Adv. Mater.*, 2016, **28**, 10016–10023.

49 J. Lee, J. W. Chung, J. Jang, D. H. Kim, J.-I. Park, E. Lee, B.-L. Lee, J.-Y. Kim, J. Y. Jung, J. S. Park, B. Koo, Y. W. Jin and D. H. Kim, *Chem. Mater.*, 2013, **25**, 1927–1934.

50 E. H. Suh, S. B. Kim, H. S. Yang and J. Jang, *Adv. Funct. Mater.*, 2022, **32**, 2207413.

51 N. Y. Kim, T. S. Lee, D. Y. Lee, J. G. Oh, K. Lee, J. Y. Kim, T. K. An, Y. J. Jeong, J. Jang and Y.-H. Kim, *J. Mater. Chem. C*, 2021, **9**, 340–347.

52 R.-X. Jhang, G.-L. Chen, R. Raja, P.-T. Chen, M. Hayashi, S.-P. Rwei, S.-h. Hsu and L. Wang, *Dyes Pigm.*, 2021, **188**, 109206.

53 E. H. Suh, Y. J. Jeong, J. G. Oh, K. Lee, J. Jung, Y. S. Kang and J. Jang, *Nano Energy*, 2019, **58**, 585–595.

54 S. E. Yoon, S. J. Shin, S. Y. Lee, G. G. Jeon, H. Kang, H. Seo, J. Zheng and J. H. Kim, *ACS Appl. Polym. Mater.*, 2020, **2**, 2729–2735.

55 E. H. Suh, M.-K. Jeong, K. Lee, W. Jeong, Y. J. Jeong, I. H. Jung and J. Jang, *Adv. Funct. Mater.*, 2022, **32**, 2207886.

56 D. A. Stanfield, Y. Wu, S. H. Tolbert and B. J. Schwartz, *Chem. Mater.*, 2021, **33**, 2343–2356.

57 D.-X. Xie, T.-C. Liu, J. Xiao, J.-K. Fang, C.-J. Pan and G. Shao, *Molecules*, 2021, **26**, 963.

58 H. Zeng, M. Mohammed, V. Untilova, O. Boyron, N. Berton, P. Limelette, B. Schmaltz and M. Brinkmann, *Adv. Electron. Mater.*, 2021, **7**, 2000880.

59 G. Zuo, H. Abdalla and M. Kemerink, *Adv. Electron. Mater.*, 2019, **5**, 1800821.

60 T. Meng, C. Yi, L. Liu, A. Karim and X. Gong, *Emergent Mater.*, 2018, **1**, 67–76.

61 U. Sreevidya, V. Shalini, K. K. Bharathi, E. S. Kumar, M. Prakash and M. Navaneethan, *J. Mater. Sci.: Mater. Electron.*, 2022, **33**, 11650–11660.

62 T. L. D. Tam, M. Lin, A. D. Handoko and J. Xu, *ACS Appl. Polym. Mater.*, 2021, **3**, 5596–5603.

63 Z. Yan, Z. Zhuxia, L. Tianbao, L. Xuguang and X. Bingshe, *Spectrochim. Acta, Part A*, 2008, **70**, 1060–1064.

64 N. Raveendran, T. Ghosh, V. Ignatious, V. Darshan, N. Jacob, B. Deb and C. Vijayakumar, *Mater. Today Energy*, 2023, **34**, 101296.

65 D. Xie, J. Xiao, Q. Li, T. Liu, J. Xu and G. Shao, *Polymers*, 2021, **13**, 2486.

66 J. Min, J. Im, S. H. Kim, H. H. Choi and K. Cho, *Adv. Funct. Mater.*, 2023, **33**, 2212825.

67 Y. Zhang, L. Deng, Y. Cho, J. Lee, N. Shibayama, Z. Zhang, C. Wang, Z. Hu, J. Wang, F. Wu, L. Chen, Y. Du, F. Ren, C. Yang and P. Gao, *Small*, 2023, **19**, e2206233.

68 O. Zapata-Arteaga, S. Marina, G. Zuo, K. Xu, B. Dörling, L. A. Pérez, J. S. Reparaz, J. Martín, M. Kemerink and M. Campoy-Quiles, *Adv. Energy Mater.*, 2022, **12**, 2104076.

9816 | *J. Mater. Chem. A*, 2024, **12**, 9806–9816

This journal is © The Royal Society of Chemistry 2024